CHEMISTRY OF MATERIALS

pubs.acs.org/cm
Article

A Unified Mechanism for Strain- and Anneal-Induced Oxygen-Vacancy Behavior in Oxide Semiconductors

Hyeongjun Jang, Yoonju Park, Beomjin Park, Taehyun Kim, Jungho Lee, Jian-Yu Lin, Chang Niu, Peide D. Ye, Ho-Hyun Nahm, and Changwook Jeong*

Cite This: Chem. Mater. 2026, 38, 6050−6058
Read Online

ACCESS | Metrics & More | Article Recommendations | Supporting Information

ABSTRACT: Oxygen vacancies (V_O) critically influence the electrical performance and reliability of amorphous oxide semiconductor (AOS) devices, including indium−gallium−zinc oxide (IGZO) thin-film transistors (TFTs). Using first-principles density functional theory and configuration-coordinate analysis, we elucidate a unified mechanism connecting the contrasting behaviors of V_O under strain versus annealing. We demonstrate that both mechanical strain and annealing-induced structural relaxation modulate the energetic position and localization character of V_O states by altering specific interatomic distances. Compressive strain shortens key metal−metal separations, thereby stabilizing bonding-like localized states, lowering their formation energy, and driving a delocalized-to-localized transition; conversely, tensile strain induces the opposite trend. Along the structural-relaxation pathway, the defect level shifts upward toward the conduction band minimum as critical distances increase, promoting delocalization. *Ab initio* molecular dynamics simulations further corroborate that higher thermal budgets facilitate this relaxation, thereby enhancing donor activation. Crucially, we resolve the prevailing apparent strain−annealing densification inconsistency: annealing-induced delocalization arises not from increased mass density (as in compressive strain), but specifically from structural relaxation that expands critical interatomic distances and minimizes screened ion−ion repulsion. These findings provide a rigorous atomistic framework for manipulating defect states via strain engineering and thermal processing, offering precise guidelines for optimizing the stability and performance of next-generation AOS electronics.

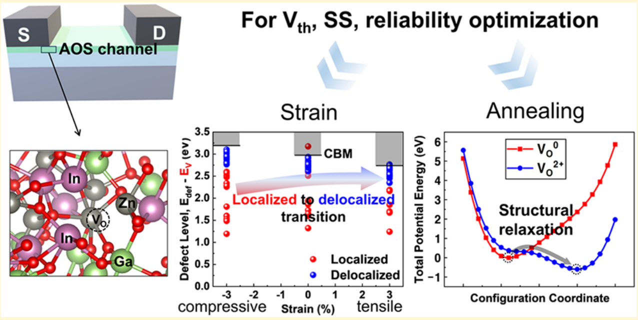

1. INTRODUCTION

Amorphous oxide semiconductors (AOSs) underpin a broad range of oxide-electronics applications, including display backplanes, transparent/low-temperature circuits, sensors, and memory/selector elements, because they combine high spatial uniformity,[1] low-temperature processability,[2] high on/off ratios,[3] and respectable mobility.[4−6] Among AOSs, indium−gallium−zinc oxide (IGZO) is a widely adopted material platform and is also considered for next-generation DRAM devices.[7] Nevertheless, defect-induced degradation in mobility, subthreshold swing (SS), and reliability remains a central challenge for achieving stable, high-performance AOS-based devices.[8−10] Therefore, it is essential to develop methods that explain and control defects governing key electrical properties—including SS, threshold voltage (V_{th}), and reliability—across this broader device landscape.

Among various defects, oxygen vacancies (V_O) are intrinsic and dominant in oxide semiconductors. Although other defects such as metal interstitials and defect complexes may also exist, oxygen vacancies are widely considered to be the predominant defect species, directly impacting the electrical behavior of oxide semiconductors. Their electronic behavior depends strongly on the local structure, acting either as localized electron traps or as delocalized donors.[11,12] Consequently, both V_O character (localized vs delocalized) and energetic level (shallow/intermediate/deep) critically affect device metrics.[13] Because these attributes are modulated by interatomic distances and the local bonding environment, device performance can be tuned by deliberately engineering defect environments.

Motivated by this perspective, prior studies on AOS devices (e.g., thin-film transistor (TFT) channels) have explored performance gains by manipulating atomic distances or bonding environments, primarily via strain or channel densification. Reports indicate that compressive strain yields a positive threshold-voltage shift ($\Delta V_{th} > 0$) and improves reliability, whereas tensile strain yields $\Delta V_{th} < 0$.[14−16] Nevertheless, although prior studies have provided valuable insights into the

Received: February 25, 2026
Revised: May 26, 2026
Accepted: June 1, 2026
Published: June 4, 2026

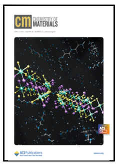

https://doi.org/10.1021/acs.chemmater.6c00577
Chem. Mater. 2026, 38, 6050−6058

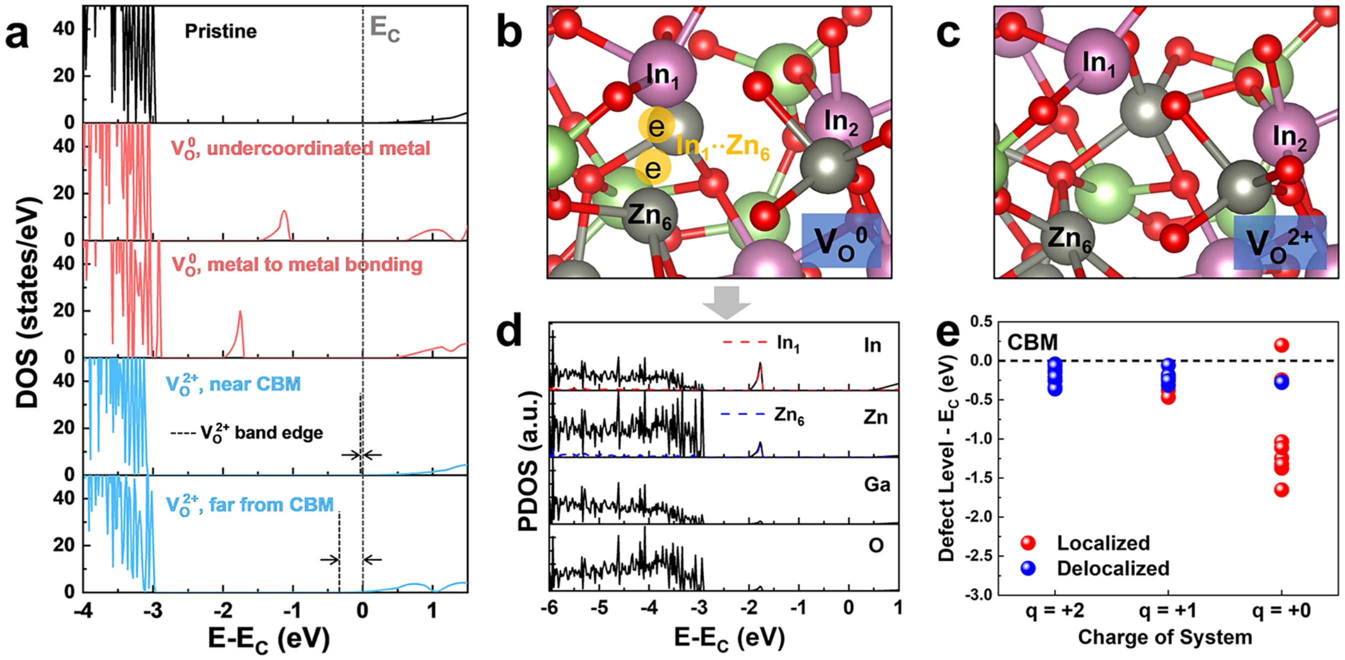

Figure 1. (a) Density of states for the pristine structure and for IGZO structures containing oxygen vacancies. The figure includes representative cases of $V_O{}^0$ associated with an undercoordinated metal site, $V_O{}^0$ originating from metal−metal bonding, and $V_O{}^{2+}$ defects located near or far from the conduction band minimum (CBM). Atomic configuration of IGZO structure with (b) localized oxygen vacancy defect and (c) delocalized oxygen vacancy defect. (d) Partial density of states of the $V_O{}^0$ localized state for each element in structure (b). The localized state originates from the bonding between In_1 and Zn_6. (e) Defect levels of $V_O{}^0$, $V_O{}^{1+}$, and $V_O{}^{2+}$ relative to CBM across ten structures.

effects of strain on amorphous IGZO,[17−19] investigations that directly address how strain modifies defect-state evolution are relatively limited. By contrast, densification has been reported to increase the fraction of delocalized states—attributed to reduced interatomic distances and free volume—thereby increasing carrier concentration and producing $\Delta V_{th} < 0$.[20−26] This presents an apparent strain−annealing densification inconsistency: densification reduces interatomic distances much like compressive strain, yet yields the opposite ΔV_{th} sign.

We resolve this inconsistency by decoupling mass-density change from structural relaxation and analyzing the configuration-coordinate (CC) pathway. By evaluating the density of states (DOS) and defect-formation energy along this pathway at a typical Fermi level for amorphous IGZO-based TFTs, we demonstrate that as the network structurally relaxes, specific interatomic distances increase and the defect level shifts toward the CBM, promoting delocalization. Moreover, decomposing the formation energy identifies the screened ionic-repulsion term (ΔU_r) that decreases along relaxation, stabilizing the delocalized configuration. Together with our ab initio molecular dynamics (AIMD) annealing simulations in the canonical (NVT) ensemble, which isolate relaxation at a fixed volume, these results indicate that annealing-driven delocalization ($\Delta V_{th} < 0$) arises primarily from structural relaxation mediated by interatomic distances (due to screened ion−ion repulsive interactions), whereas mechanical strain modulates defect energetics through interatomic-distance changes (due to metal−metal hybridized interactions); the same mechanism governs both cases, distinguished only by their driving forces. This insight provides a refined interpretation beyond the conventional view,[20−26] which has typically attributed delocalization only to increased mass density and reduced free volume.

Although our computations and target materials are presented for IGZO and interpreted in the context of TFT-style channels, the underlying mechanism depends only on local structural descriptors—interatomic-distance evolution along the CC and the ΔU_r—rather than on device architecture. We therefore expect the trends to generalize across other AOS compositions and oxide-electronics contexts in which V_O donation and state localization set operating margins (e.g., display backplanes, sensors, and selector/memristive stacks). Using density functional theory (DFT) together with CC analysis, we quantify V_O responses to strain and annealing-induced relaxation and identify a unified distance-driven mechanism that resolves prior inconsistencies and informs process strategies to control key electrical properties in AOS devices. We note that the present work does not aim to exhaustively cover all possible defect species, and the potential roles of other defects are subjects for future investigation.

2. RESULTS AND DISCUSSION

2.1. Electronic Nature of Oxygen Vacancies: Localization vs Delocalization

Figure 1a presents a comparative analysis of the DOS for the pristine structure alongside two representative V_O configurations: a delocalized $V_O{}^{2+}$ state and a localized $V_O{}^0$ state. For $V_O{}^{2+}$, the defect level appears as a shallow state near the conduction band minimum (CBM); depending on the local configuration, it ranges from nearly degenerate with the CBM to ≈0.3 eV below it. By contrast, $V_O{}^0$ exhibits a deep localized state associated with metal−metal bonding. Note that not all electron-trapping states are necessarily deep: when electrons are concentrated on a single undercoordinated metal, the defect level can shift upward toward higher energy.[27] Electrically, when the two excess electrons associated with an oxygen vacancy are donated to the CBM ($V_O{}^{2+} + 2e^-$ at CBM), the vacancy adopts the ionized donor state $V_O{}^{2+}$, increasing the carrier concentration and

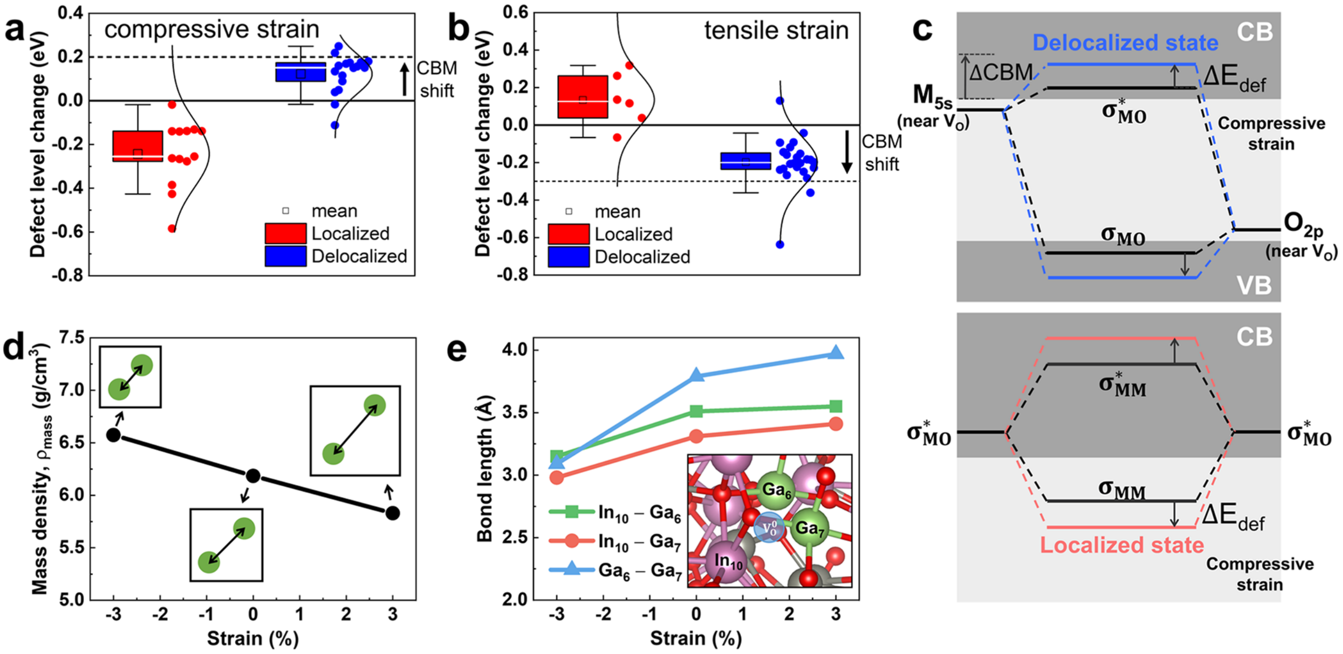

Figure 2. Box plots and distributions of absolute shifts in defect levels when (a) compressive and (b) tensile strain are applied. The black dotted line indicates the CBM shift in the pristine structure. Delocalized states shift in the same direction as the pristine CBM, whereas localized states shift in the opposite direction. (c) Schematic diagram illustrating how M−M and M−O bond length contraction shifts σ_{MM} and σ^*_{MO} states, thereby shifting the defect states upward or downward in energy. This diagram illustrates one representative case of bonding and antibonding states near V_O. (d) Mass-density variation under compressive and tensile strain. Atomic distances decrease under compressive strain and increase under tensile strain due to unit-cell expansion. (e) Bond length evolution under biaxial strain for a representative structure with an oxygen vacancy (inset). The metal−metal bond lengths increase progressively with tensile strain.

producing $\Delta V_{th} < 0$. Conversely, when these two electrons remain localized in a vacancy-related defect state, the vacancy remains in the neutral $V_O{}^0$ state ($V_O{}^0 = V_O{}^{2+} + 2e^-$ at in-gap defect level), acting as an electron-trapping configuration that lowers the free carrier density and yields $\Delta V_{th} > 0$. Figure 1b and c show that shorter metal−metal (M−M) distances favor localized states, whereas longer M−M distances favor delocalized states, establishing a clear correlation between structural configuration and the electronic nature of defect states. Consistently, the partial density of states (PDOS) in Figure 1d indicates that the deep localized state arises from In−Zn bonding in Figure 1b. Figure 1e summarizes the defect levels and charge states ($q = 0, +1, +2$) across ten distinct amorphous configurations, highlighting the structural diversity inherent in AOS.

2.2. Nature of Strain-Induced Defect Modulation

To probe the sensitivity of these defect states to strain, we applied the ± 3% in-plane biaxial strain and quantified the absolute shifts of defect levels, as shown in Figure 2a and b. Notably, localized and delocalized levels shift in opposite directions under the same strain. This behavior can be rationalized by the distinct active bonding models illustrated in Figure 2c: delocalized and localized states derive from strengthened metal−oxygen hybridization (characterized by larger splitting between bonding (σ_{MO}) and antibonding (σ^*_{MO}) states) and created metal−metal $\sigma^*_{MO} - \sigma^*_{MO}$ hybridization (σ_{MM}) between two metal σ^*_{MO} orbitals, respectively. Under compression, decreasing interatomic separations raise the energy of M−O antibonding states,[18,19,28] so both the delocalized level and the pristine CBM shift upward; simultaneously, shorter M−M distances stabilize (lower) the M−M bonding level, deepening localized states. Tensile strain reverses these trends, lowering delocalized levels while raising localized levels. These opposite responses encode the distinct bonding origins of the two defect types. It should be noted that the present interpretation is mainly concerned with local defect-state evolution driven by short-range bonding changes. By contrast, the CBM behavior in amorphous structures may also be influenced by medium-range order and system-size effects, which are not fully reflected in the current model.[17]

Figure 2d shows the variation of mass density as a function of strain: tensile strain expands the in-plane cell (reducing density and increasing atomic distances), while compressive strain contracts it (increasing density and shortening atomic distances). These strain-induced distance changes drive the level shifts in both localized and delocalized states described above. As a result, transitions between localized and delocalized states can occur as the local M−M bond length near the oxygen vacancy changes. In Figure 2e, the M−M distance increases monotonically from compressive to tensile strain; in this representative structure, the oxygen vacancy tends to be localized under compression but to be delocalized under tension. This confirms that the transition from a localized state to a delocalized state under tensile strain is governed by the strain-induced increase in M−M bond length near the vacancy.

Figure 3a summarizes the evolution of defect levels under strain, including the concurrent bandgap change. Under tensile strain, the bandgap narrows as the CBM shifts downward (~0.19 eV) and the VBM shifts upward (~0.05 eV); under compressive strain, the opposite trend is observed. Consequently, tensile strain generally brings defect levels closer to the CBM in absolute energy, while compressive strain moves them away. Figure 3b shows defect-level shifts referenced to the CBM (i.e., $\Delta E \equiv E_{def} - E_C$) and excludes cases in which a defect

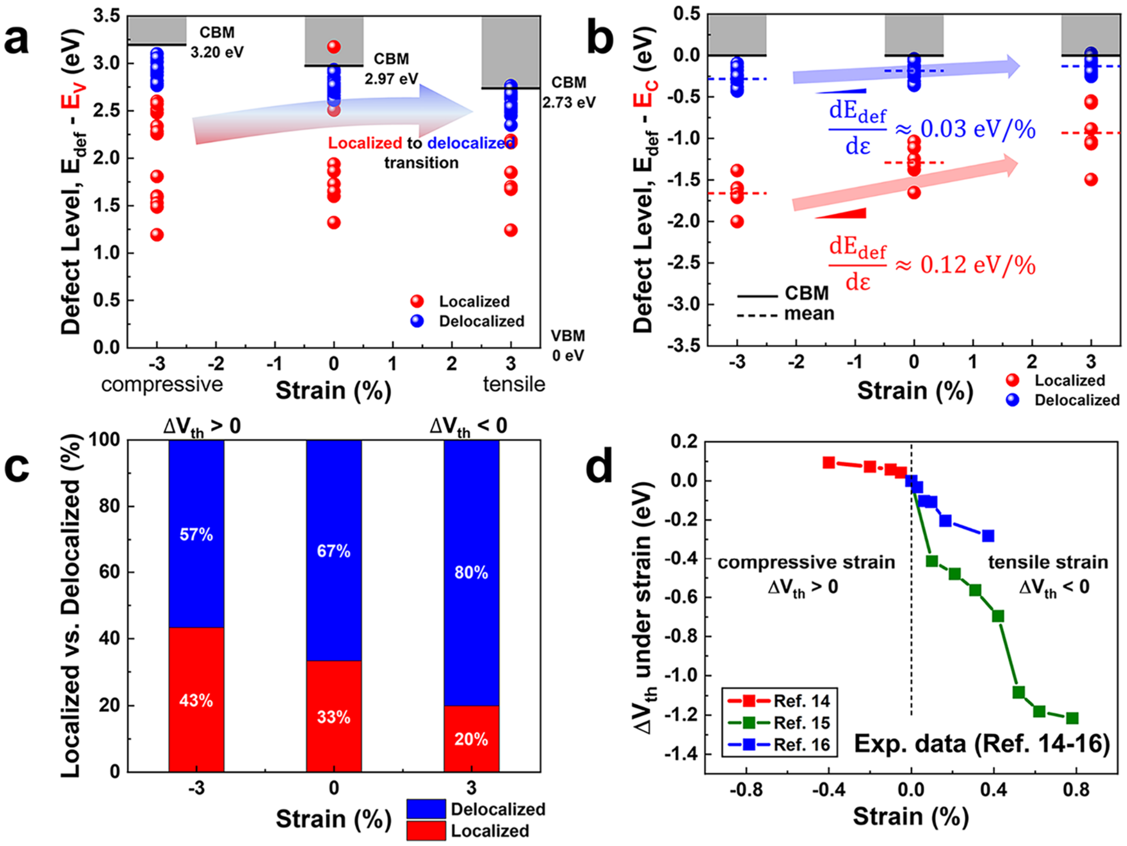

Figure 3. (a) Variation of defect levels and types under compressive and tensile strain, with the corresponding bandgap change. It indicates that applying biaxial strain modulates defect levels and, in some cases, even the defect type. (b) Defect-level shifts relative to the CBM under strain, excluding the localized to delocalized transition. The slope represents the rate of defect level shift with respect to applied strain (eV/%). The slope is 0.12 eV/% for localized states and 0.03 eV/% for delocalized states. (c) Percentage change of delocalized (blue) and localized (red) states as a function of strain. Under tensile strain, localized states are converted into delocalized states, which causes $\Delta V_{th} < 0$. In contrast, compressive strain leads to the opposite trend. (d) Experimental data of ΔV_{th} under applied strain, from refs 14−16. The experimental results show $\Delta V_{th} > 0$ under compressive strain and negative shifts under tensile strain, consistent with our DFT simulation results.

state changes character (localized ↔ delocalized). The calculated rates of defect-level change with strain are ≈0.03 eV/% for delocalized states and ≈0.12 eV/% for localized states. As tensile strain increases, both localized and delocalized states increase (they track upward relative to the CBM), consistent with the CBM's stronger downward movement under tension.

When a localized level is raised sufficiently close to the CBM under tensile strain, it can convert to a delocalized state; the reverse transition occurs under compression, as illustrated in Figure 3c. Under compressive strain, the fraction of localized states increases from 33% to 43%, while the delocalized fraction decreases from 67% to 57%. Under tensile strain, the localized fraction decreases to 20%, and the delocalized fraction increases to 80%. These opposite responses reflect the distinct bonding origins (M−M bonding versus M−O bonding) discussed in Figure 2. Additionally, In_2O_3 shows an analogous qualitative response under biaxial in-plane strain: the defect-state energetics shift in the same direction and the localization tendency follows the same overall trend as in IGZO (see SI Section 1 and Figure S1).

The experimental data in Figure 3d follow the same trend: $\Delta V_{th} < 0$ under tensile strain and $\Delta V_{th} > 0$ under compressive strain. Crucially, the strain effect is 2-fold: (i) it can change the defect type distribution (localized ↔ delocalized), and (ii) it systematically shifts defect energies themselves. Hence, the peak positions of subgap states are tunable via the atomistic bonding environment.

2.3. Resolving the Apparent Strain Annealing Densification Inconsistency: The Role of Structural Relaxation

Superficially, the strain results appear to contradict the phenomenon of "densification," where film annealing—which reduces free volume and increases mass density—is reported to enhance delocalization ($\Delta V_{th} < 0$).[20−26] In our in-plane, fixed-out-of-plane strain protocol, compressive strain increases the mass density by ∼6%, shortens interatomic distances, favors localization, and yields $\Delta V_{th} > 0$—the opposite sign. This apparent strain−annealing densification inconsistency indicates that the experimentally observed enhancement of delocalized states during annealing densification is not caused by mass density increase alone. Rather, our results point to structural relaxation as the primary driver: delocalization arises during annealing when metal ions gain sufficient thermal energy to separate along the CC, stabilizing the delocalized state. The mechanism is the same CC picture identified in the strain study; what differs is the driving force (mechanical strain vs thermally driven relaxation), thereby reconciling the two observations.

To analyze structural relaxation in more detail, when the Fermi level (E_F) is lower than the thermodynamic charge transition level (CTL) (∼0.29 eV), we constructed CC diagrams. Figure 4a illustrates the formation-energy surfaces of V_O^0 and V_O^{2+} as a function of the CC. The two surfaces cross

https://doi.org/10.1021/acs.chemmater.6c00577
Chem. Mater. 2026, 38, 6050−6058

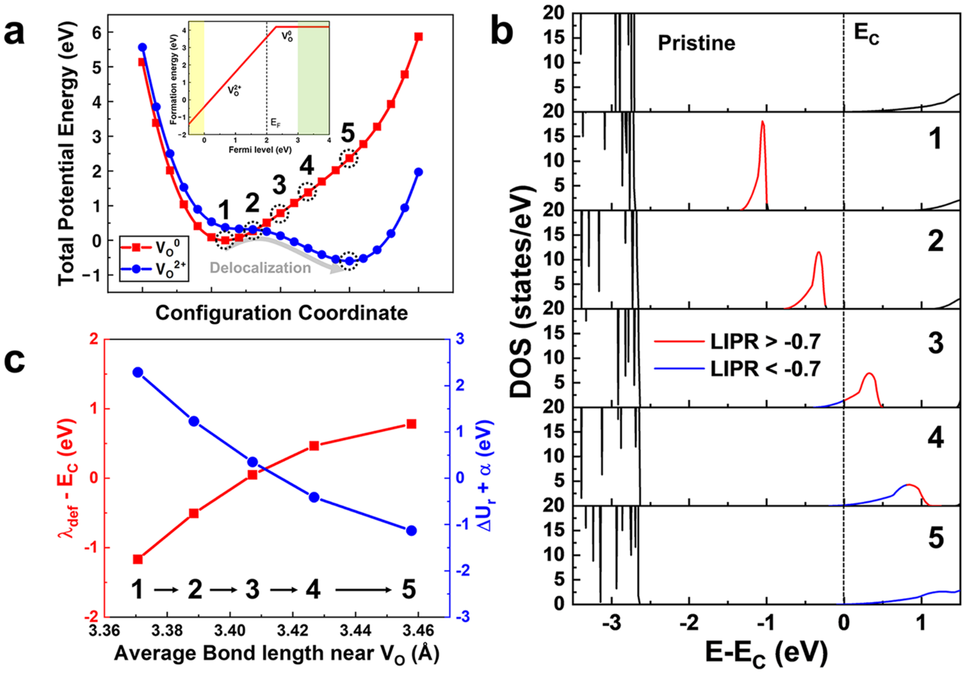

Figure 4. (a) Potential energy profiles of V_O^{2+} (blue) and V_O^0 (red) defect states as a function of the configuration-coordinates, showing the activation barrier associated with structural reconfiguration. The inset figure shows the oxygen vacancy defect formation energy as a function of the Fermi level. In this case, the Fermi level is set to 2 eV, so V_O^{2+} is more stable than V_O^0. (b) Defect states change in DOS from configuration 1 to 5. As the structure evolves from configuration 1 to 5, the defect states move upward in the DOS, accompanied by a reduction in LIPR, signifying progressive delocalization. The LIPR values are computed in accordance with the definition provided in ref 29. (c) Changes in eigenvalues and ΔU_r depending on the average bond length of metals near V_O along configurations 1−5.

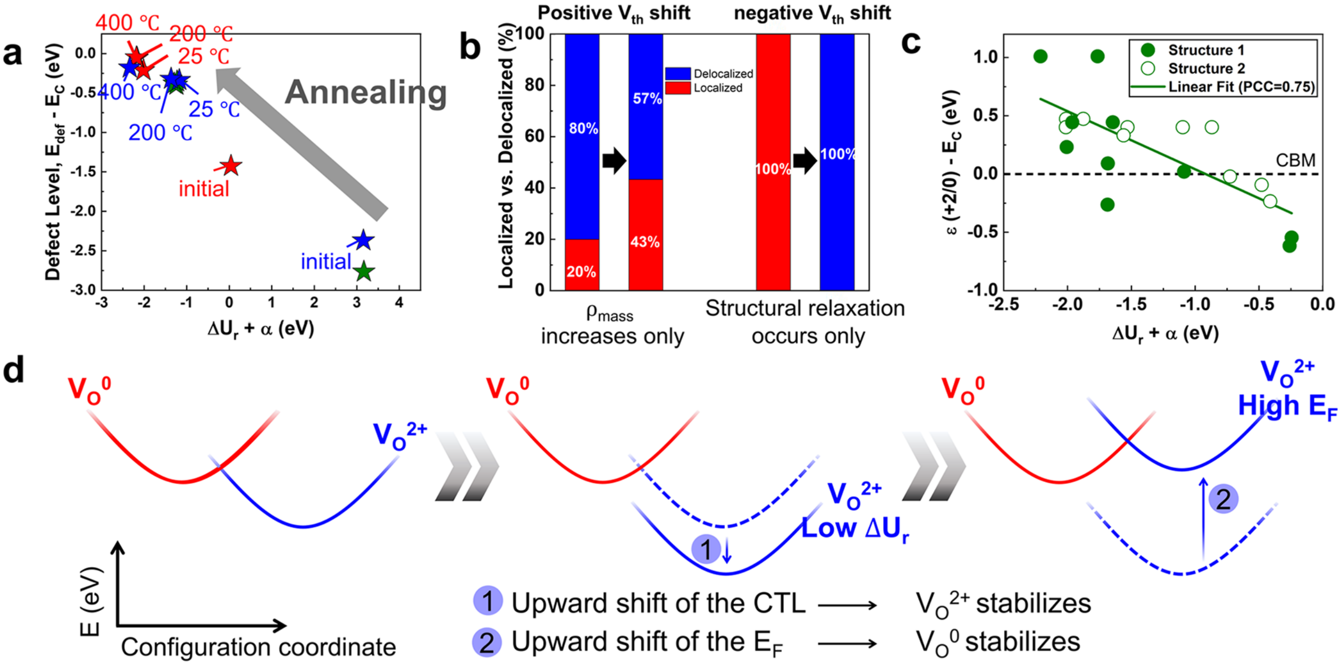

Figure 5. (a) Changes in ΔU_r and defect levels during annealing simulation. Higher annealing temperature makes ΔU_r more stable and defect levels closer to CBM. (b) Percentages of localized and delocalized states when only mass density increases or only structural relaxation occurs. (c) Charge transition level, $\varepsilon(+2/0)$, as a function of ΔU_r. For the pooled data set, the Pearson correlation coefficient (PCC) is 0.75. When fitted separately, Structure 1 and Structure 2 yield PCC values of 0.80 and 0.83, respectively (see SI Section S9 and Figure S5). (d) Schematic illustration of the configuration-coordinate diagrams of V_O^0 and V_O^{2+} under structural relaxation. The shifts in the CTL and the E_F determine whether the localized or delocalized state is energetically favored under each condition.

with an activation energy barrier (∼0.31 eV) for the transition from V_O^0 to V_O^{2+}, indicating that the transition to the more stable V_O^{2+} state requires sufficient energy to overcome this barrier. During annealing, thermal energy enables barrier crossing and drives the system from the localized V_O^0 minimum to the delocalized V_O^{2+} minimum.

Table 1. Comparison of Experimental Observations and the Interpretation Proposed in This Study for Strain and Thermal Annealing Effects[a]

	Strain		Thermal annealing	
	Compressive	Tensile	Bandgap	ΔV_{th}
Observation	$\Delta V_{\text{th}} > 0$	$\Delta V_{\text{th}} < 0$	Increase	$\Delta V_{\text{th}} < 0$
Interpretation in prior studies	Often discussed in terms of bandgap changes	Attributed mainly to changes in gate-dielectric charge states	Explained by the reduction of tail/subgap states	Typically associated with densification during annealing
Unified interpretation proposed in this study	A unified distance-driven evolution of V_O states explains both strain- and annealing-induced changes in V_{th} and bandgap: longer distances favor V_O^{2+} states near the CBM, whereas shorter distances favor V_O^0 states deeper below the CBM.			
Consistency with the experiment	Yes	Yes	Yes	Yes

[a] ΔV_{th} denotes the threshold-voltage shift.

To resolve the atomistic pathway, we sampled five representative configurations along the CC path connecting the localized and delocalized states (configuration index, Q from Q_1 to Q_5). The corresponding DOS in Figure 4b shows that defect levels starting near midgap shift upward and eventually merge with the CBM. We quantify orbital localization using the log-scaled inverse participation ratio (LIPR);[29] we classify eigenstates with LIPR > −0.7 as localized (red) and those with LIPR < −0.7 as delocalized (blue), where lower LIPR indicates greater spatial delocalization. Consistently, as the defect level rises, the LIPR value decreases, indicating delocalization. As demonstrated in Figure 4c, the average M−M bond length near V_O also increases from Q_1 to Q_5. Thus, the delocalization that develops during annealing follows the same structure−electronic link identified under strain: increasing key interatomic distances pushes the defect level upward (toward the CBM) and promotes delocalization. In other words, annealing and tensile strain activate the same CC mechanism; the distinction lies in the driving force (thermal vs mechanical).

A remaining question is why the system adopts a delocalized configuration even though the defect eigenvalue typically rises along the path. To clarify this behavior, we decompose the defect formation energy as

$$E_{\text{form}} \sim \lambda_{\text{def}} + \Delta U_r + \alpha \tag{1}$$

following the tight-binding-based expression ($E_{\text{tot}} = 2\sum_{i,\text{occ}} \lambda + U_r$)[30,31] (Details in Supporting Information Section 2). Here, λ_{def} is the electronic (eigenvalue) contribution associated with occupying the defect state, ΔU_r is the screened ionic-repulsive interaction term governed by the atomic arrangement, and collects configuration-independent constant parameters of the formation energy ($\alpha = \mu_O + E_{\text{corr}}(q) + q(E_F + E_V)$). As the system evolves from Q_1 to Q_5 in Figure 4c, λ_{def} increases, but ΔU_r decreases sufficiently—reflecting reduced short-range ion−ion repulsion as the network opens—so that the net E_{form} drops and the delocalized state is stabilized. This energy-component trade-off reconciles the upward shift of the defect level with the thermodynamic preference for the delocalized configuration.

AIMD annealing further corroborates the structural-relaxation picture. As shown in Figure 5a, initially localized states become delocalized upon annealing, with structural relaxation as the primary driver. Increasing the anneal temperature allows the system to explore lower-energy configurations: the screened ionic-repulsive interaction term ΔU_r decreases, and the delocalized defect level moves upward toward the CBM. At 25 °C, defect levels remain sufficiently below the CBM, limiting the donor contribution of even delocalized states; after anneals at 200 °C and 400 °C, the levels approach the CBM and contribute more strongly to carrier generation. This trend is consistent with experiments reporting increased carrier concentration at higher annealing temperatures[32,33] and optical bandgap widening without changes in crystalline fraction.[34]

The AIMD simulations were performed in the NVT ensemble, fixing the cell volume and thereby suppressing net density change; the observed evolution therefore reflects structural relaxation only. Figure 5b compares two protocols: (i) mass-density increase only and (ii) structural relaxation only. The comparison indicates that the commonly observed $\Delta V_{\text{th}} < 0$ during annealing densification is primarily attributed to relaxation-induced delocalization, rather than to mass density increase itself. In other words, increases in key interatomic distances during relaxation drive delocalization, refining earlier interpretations that linked delocalization directly to higher mass density (and reduced free volume). To summarize the distinction between experimental observations, the conventional interpretation, and the mechanism proposed in this work, Table 1 compares the strain- and annealing-induced trends in ΔV_{th} and bandgap. It also highlights how the apparent strain−annealing densification inconsistency is resolved in this study.

Structural relaxation does not always induce net delocalization. When E_F is high or the CTL is low, the localized V_O^0 state can be thermodynamically favored. During relaxation, both CTL and E_F evolve, producing repeated localization−delocalization cycles. As shown in Figure 5c, a decrease in ΔU_r raises the CTL (see SI Section 3), stabilizing the V_O^{2+} and promoting delocalization (process (1) in Figure 5d). Simultaneously, either delocalization itself or an upward shift of the delocalized level toward the CBM increases carrier density, which in turn raises E_F; a higher E_F can then favor V_O^0 and promote relocalization (process (2) in Figure 5d). This feedback loop continues until ΔU_r reduction saturates and a quasi-equilibrium is reached. Consequently, even under prolonged annealing, not all oxygen vacancy states become fully delocalized; the coexistence of localized and delocalized states imposes an intrinsic limit on the achievable carrier density. These interpretations provide an atomistic perspective on the phenomena that emerge during densification under realistic processing conditions.

Finally, to connect atomistic trends to device observables, an incremental donor sheet charge ΔQ_d from delocalized V_O^{2+} produces a threshold shift $\Delta V_{\text{th}} \approx -\Delta Q_d / C_{OX}$ for a given gate stack. This provides a direct route to map strain- or structural-relaxation-driven defect-state modulation onto ΔV_{th} targets in IGZO TFTs and related AOS devices.

3. CONCLUSION

We performed an atomistic analysis of oxygen vacancies in AOS and showed that local interatomic distances and bonding environments determine both the localization character (localized vs delocalized) and the energetic depth (shallow/intermediate/deep) of the defect state. From this picture, we identify two practical levers for engineering the defect levels and types in oxide semiconductors. First, strain modifies interatomic distances and shifts defect levels in ways predictable from the underlying bonding characteristics. Second, annealing-induced structural relaxation reconfigures the network toward lower-energy arrangements, often increasing key metal−metal distances and favoring donor delocalization.

These two levers operate through a single CC mechanism: variations in the critical interatomic distance set both the defect-level position relative to the CBM and the degree of state localization. The accompanying AIMD simulations, performed at a fixed volume, isolate structural relaxation from net density change and refine the conventional interpretation that attributed defect-state delocalization to increased mass density or reduced free volume; instead, structural relaxation during annealing is the dominant driver.

Taken together, the DFT and AIMD results provide mechanistic guidance for tuning V_{th}, SS, and reliability and offer process-level direction for oxide-electronics devices, including—but not limited to—IGZO-based TFTs, sensors, and selector/memristive elements.

4. COMPUTATIONAL METHODS

4.1. DFT Calculation for IGZO Structures with Defects

We prepared IGZO (In:Ga:Zn = 1:1:1) structures using our in-house developed machine learning potential (MLP)[35,36] and generated 10 structures by introducing oxygen vacancies at ten distinct sites within the same parent structure. The parent amorphous IGZO supercell used in this study contains 77 atoms with lattice parameters of 9.74 Å. We efficiently screened oxygen vacancies and identified low-energy candidates using the QuantumATK software.[37] We note that the present sampling and screening do not reproduce the entire defect population formed under sputtering conditions or fully capture the structural variability present in experimentally synthesized IGZO. Nevertheless, they are sufficient for examining the qualitative evolution of defect states under strain and annealing. Accordingly, the present study is intended to establish a mechanism-level trend rather than a statistically converged defect distribution under realistic growth conditions. For each structure, we computed three charge states of the oxygen vacancy (V_O^0, V_O^{1+}, and V_O^{2+}) and evaluated the corresponding defect levels. In this work, the term defect level specifically denotes the Kohn−Sham defect eigenvalue associated with the oxygen vacancy state. Three charge states were obtained by removing electrons from the supercell. Specifically, two electrons were removed for V_O^{2+}, one for V_O^{1+} and none for V_O^0. To probe strain effects, we applied in-plane biaxial tensile and compressive strains of ± 3% with the out-of-plane lattice held fixed (see Supporting Information S4) and recomputed the defect electronic structure. For annealing studies, AIMD simulations were performed in the NVT ensemble, which keeps the cell volume fixed and thereby isolates structural-relaxation effects from mass-density change. For each target temperature, the system was heated, equilibrated for 10 ps ($T = 25-400$ °C) to ensure sufficient annealing, and then quenched to 300 K. This protocol enabled us to isolate the role of structural relaxation without coupling it to mass density changes. DFT calculations were performed using the Vienna Ab initio Simulation Package (VASP).[38] All calculations used consistent convergence criteria for k-mesh and cutoff values across strain and charge state conditions to ensure comparability. Detailed DFT parameters and settings are provided in Supporting Information S5.

4.2. Defect Formation Energy and Repulsive Energy between Ions

The ΔU_r represents the change in the screened repulsive energy between ions in the defect formation energy, clearly separated from the contribution arising purely from electronic eigenstate energy. We estimated it by calculating the defect formation energy after removing two electrons from the supercell (charge state $q = +2$) while atoms were fixed at the previously optimized structure. This procedure is equivalent to evaluating the DOS and formation energy of the V_O^{2+} charge state. More details about ΔU_r are provided in Supporting Information S2. Defect formation energies were calculated using the doped package with standard chemical potential references and the extended Freysoldt−Neugebauer−Van de Walle (eFNV) correction for charged defects (image-charge plus potential-alignment).[39,40] More details about the setting of defect formation energy calculations are provided in Supporting Information S6. The CC diagram for the oxygen vacancy was constructed by linearly interpolating atomic positions between the fully relaxed geometries of the V_O^0 and V_O^{2+} charge states. For each intermediate structure, single-point energy calculations were performed for both charge states to obtain the adiabatic potential energy surfaces. Because V_O exhibits negative-U behavior, the V_O^{1+} state was omitted, and the transition from the neutral to the doubly positive charge state was considered directly.[41] The activation barrier and structural relaxation energy were then extracted from the resulting energy profiles.

■ ASSOCIATED CONTENT

Supporting Information

The Supporting Information is available free of charge at https://pubs.acs.org/doi/10.1021/acs.chemmater.6c00577.

(S1) The defect trend for In_2O_3 under ± 3% biaxial strain; (S2) repulsive energy between ions (ΔU_r) in defect formation energy; (S3) linear correlation between ΔU_r and oxygen vacancy CTL; (S4) settings of strain calculation; (S5) DFT settings of DOS calculation and defect states calculation; (S6) the details about oxygen vacancy defect formation energy calculations; (S7) identification of localized V_O^0 states using IPR and DOS calculation; (S8) changes in bandgap (ΔE_g) and effective mass (Δm^*) of IGZO (In:Ga:Zn = 5:1:1) under uniaxial and biaxial strain; (S9) PCC values obtained by separately fitting in Structure 1 and Structure 2 data; (S10) RDF of amorphous structures used in calculation; (S11) effect of cation species on oxygen vacancy defect states; (S12) details of the machine learning potential (PDF)

■ AUTHOR INFORMATION

Corresponding Author

Changwook Jeong − *Graduate School of Semiconductor Materials and Devices Engineering, Ulsan National Institute of Science and Technology, Ulsan 44919, Republic of Korea;* orcid.org/0000-0003-3962-7153; Email: changwook.jeong@unist.ac.kr

Authors

Hyeongjun Jang − *Graduate School of Semiconductor Materials and Devices Engineering, Ulsan National Institute of Science and Technology, Ulsan 44919, Republic of Korea;* orcid.org/0009-0003-1455-7395

Yoonju Park − *Graduate School of Semiconductor Materials and Devices Engineering, Ulsan National Institute of Science and Technology, Ulsan 44919, Republic of Korea*

Beomjin Park − *Graduate School of Semiconductor Materials and Devices Engineering, Ulsan National Institute of Science and Technology, Ulsan 44919, Republic of Korea*

Taehyun Kim − *Graduate School of Semiconductor Materials and Devices Engineering, Ulsan National Institute of Science and Technology, Ulsan 44919, Republic of Korea;* orcid.org/0009-0009-0414-1226
Jungho Lee − *Graduate School of Semiconductor Materials and Devices Engineering, Ulsan National Institute of Science and Technology, Ulsan 44919, Republic of Korea*
Jian-Yu Lin − *Elmore Family School of Electrical and Computer Engineering, Purdue University, West Lafayette, Indiana 47907, United States;* orcid.org/0000-0002-8800-8714
Chang Niu − *Elmore Family School of Electrical and Computer Engineering, Purdue University, West Lafayette, Indiana 47907, United States;* orcid.org/0000-0003-3175-7164
Peide D. Ye − *Elmore Family School of Electrical and Computer Engineering, Purdue University, West Lafayette, Indiana 47907, United States;* orcid.org/0000-0001-8466-9745
Ho-Hyun Nahm − *Department of Physics, Korea Advanced Institute of Science and Technology (KAIST), Daejeon 34141, Republic of Korea;* orcid.org/0000-0002-8096-1076

Complete contact information is available at:
https://pubs.acs.org/10.1021/acs.chemmater.6c00577

Author Contributions

The manuscript was written through the contributions of all authors. All authors have given approval to the final version of the manuscript.

Notes

The authors declare no competing financial interest.

■ ACKNOWLEDGMENTS

This work was supported by the Nano & Material Technology Development Program through the National Research Foundation of Korea, funded by the Ministry of Science and ICT (2710089547). The authors also acknowledge financial support from Samsung Electronics (IO260312-15874-02) and from the Samsung Research Funding & Incubation Center for Future Technology (SRFC-IT2502-01).

■ ABBREVIATIONS

AOS, amorphous oxide semiconductor; IGZO, indium−gallium−zinc oxide; SS, subthreshold swing; V_{th}, threshold voltage; V_O, oxygen vacancy; TFT, thin-film transistor; ΔV_{th}, threshold voltage shift; CC, configuration-coordinate; DOS, density of states; ΔU_r, screened ionic-repulsion term; AIMD, ab initio molecular dynamics; NVT, canonical; DFT, density functional theory; CBM, conduction band minimum; M−M, metal−metal; PDOS, partial density of state; σ_{MO}, metal−oxygen bonding state; $\sigma_{MO}{}^*$, metal−oxygen antibonding state; σ_{MM}, metal−metal hybridization bonding state; E_F, Fermi level; CTL, charge transition level; LIPR, log-scaled inverse participation ratio; MLP, machine learning potential; VASP, Vienna ab initio simulation package

■ REFERENCES

(1) Park, J. S.; Maeng, W. J.; Kim, H. S.; Park, J. S. Review of Recent Developments in Amorphous Oxide Semiconductor Thin-Film Transistor Devices. *Thin Solid Films* **2012**, *520* (6), 1679−1693.

(2) Troughton, J.; Atkinson, D. Amorphous InGaZnO and Metal Oxide Semiconductor Devices: An Overview and Current Status. *J. Mater. Chem. C* **2019**, *7* (40), 12388−12414.

(3) Yabuta, H.; Sano, M.; Abe, K.; Aiba, T.; Den, T.; Kumomi, H.; Nomura, K.; Kamiya, T.; Hosono, H. High-Mobility Thin-Film Transistor with Amorphous $InGaZnO_4$ Channel Fabricated by Room-Temperature RF-Magnetron Sputtering. *Appl. Phys. Lett.* **2006**, *89*, No. 112123.

(4) Sheng, J.; Hong, T.; Lee, H.-M.; Kim, K.; Sasase, M.; Kim, J.; Hosono, H.; Park, J.-S. Amorphous IGZO TFT with High Mobility of ∼ 70 $cm^2/(V·s)$ via Vertical Dimension Control Using PEALD. *ACS Appl. Mater. Interfaces* **2019**, *11*, 40300−40309.

(5) Lin, Z.; Niu, C.; Jang, H.; Kim, T.; Zhang, Y.; Wang, H.; Jeong, C.; Ye, P. D. In *Enhancement of In2O3 Field-Effect Mobility up to 152 cm2·V−1·s−1 Using HZO-Based Higher-k Linear Dielectric*, 2024 IEEE Symposium on VLSI Technology and Circuits; IEEE, 2024; pp 1−2.

(6) Lee, J.; Choi, C. H.; Kim, T.; Hur, J.; Kim, M. J.; Kim, E. H.; Lim, J. H.; Kang, Y.; Jeong, J. K. Hydrogen-Doping-Enabled Boosting of the Carrier Mobility and Stability in Amorphous IGZTO Transistors. *ACS Appl. Mater. Interfaces* **2022**, *14*, 57016−57027.

(7) Li, Q.; Hu, Q.; Zhu, S.; Zeng, M.; Zhao, W.; Wu, Y. 3D Stacked IGZO 2T0C DRAM Array with Multibit Capability for Computing-in-Memory Applications. *Sci. Adv.* **2025**, *11* (21), No. eadu4323.

(8) Cho, H.; Tsuji, M.; Ueda, S.; Kim, J.; Hosono, H. Oxygen Defects and Instability in Very Thin a-IGZO TFTs. *Adv. Electron. Mater.* **2025**, *11* (15), No. e00349.

(9) Nomura, K.; Kamiya, T.; Hosono, H. Highly Stable Amorphous In-Ga-Zn-O Thin-Film Transistors Produced by Eliminating Deep Subgap Defects. *Appl. Phys. Lett.* **2011**, *99* (5), No. 053505.

(10) Chen, W.-T.; Lo, S.-Y.; Kao, S.-C.; Zan, H.-W.; Tsai, C.-C.; Lin, J.-H.; Fang, C.-H.; Lee, C.-C. Oxygen-Dependent Instability and Annealing/Passivation Effects in Amorphous In−Ga−Zn−O Thin-Film Transistors. *IEEE Electron Device Lett.* **2011**, *32* (11), 1552−1554.

(11) Mativenga, M.; Haque, F.; Billah, M. M.; Um, J. G. Origin of Light Instability in Amorphous IGZO Thin-Film Transistors and Its Suppression. *Sci. Rep.* **2021**, *11*, No. 14618.

(12) de Jamblinne de Meux, A.; Pourtois, G.; Genoe, J.; Heremans, P. Defects in Amorphous Semiconductors: The Case of Amorphous Indium Gallium Zinc Oxide. *Phys. Rev. Appl.* **2018**, *9* (5), No. 054039.

(13) Hong, H.; Jeong, K. S.; Lim, J. H.; Son, K. S.; Chung, K. B. Quantitative Analysis of Defect States in Amorphous InGaZnO Thin-Film Transistors Using Photoinduced Current Transient Spectroscopy. *J. Appl. Phys.* **2021**, *130* (1), No. 015101.

(14) Vishwakarma, K.; Lee, K.; Kruv, A.; Chasin, A.; van Setten, M. J.; Pashartis, C.; Okudur, O. O.; Gonzalez, M.; Rassoul, N.; Belmonte, A.; Kaczer, B. In *Impact of Mechanical Stress on IGZO TFTs: Enhancing PBTI Degradation*, IEEE International Reliability Physics Symposium (IRPS); IEEE, 2025; pp 1−6.

(15) Khan, S. A.; Kuo, P. C.; Jamshidi-Roudbari, A.; Hatalis, M. In *Effect of Uniaxial Tensile Strain on Electrical Performance of Amorphous IGZO TFTs and Circuits on Flexible Metal Foils*, 68th Device Research Conference; IEEE, 2010; pp 119−120.

(16) Lin, C.-Y.; Chien, C.-W.; Wu, C.-C.; Yeh, Y.-H.; Cheng, C.-C.; Lai, C.-M.; Yu, M.-J.; Leu, C.-M.; Lee, T.-M. Effects of Mechanical Strains on the Characteristics of Top-Gate Staggered a-IGZO Thin-Film Transistors Fabricated on Polyimide-Based Nanocomposite Substrates. *IEEE Trans. Electron. Devices* **2012**, *59* (7), 1956−1962.

(17) Shin, E.-C.; Kim, R.; Lee, S.-H.; Kim, H.-D. Hidden Hypernetwork and Homology in Vitrification of Ionic Oxides. *ACS Mater. Lett.* **2025**, *7*, 3497−3503.

(18) de Jamblinne de Meux, A.; Pourtois, G.; Genoe, J.; Heremans, P. Comparison of the Electronic Structure of Amorphous versus Crystalline Indium Gallium Zinc Oxide Semiconductor: Structure, Tail States and Strain Effects. *J. Phys. D: Appl. Phys.* **2015**, *48*, No. 435104.

(19) Cha, S.-K.; Im, S.; Kim, Y.-S.; Baeck, J.; Noh, J.; Park, K.-S.; Kim, J. J.; Yoon, S.-Y. Density-Dependent Microstructures and Electromechanical Properties of Amorphous $InGaZnO_4$ Semiconductors: An Ab Initio Study. *ACS Appl. Electron. Mater.* **2022**, *4*, 2545−2551.

(20) Kuo, Y.-H.; Zhang, C.; Ravikumar, P. G.; Kang, S.; Song, T.; Villena, M. A.; Larcher, L.; Kim, H.; Hong, M.; Yun, P.; Thareja, G.; Yu, S.; Ha, D.; Datta, S.; Medvedeva, J. E.; Khan, A. I. In *Experiments and Modeling of Defect Dynamics and BTI in Doped In2O3 TFTs Undergoing Densification during 400 °C Post-BEOL Forming Gas Annealing (FGA),*

2025 IEEE International Electron Devices Meeting (IEDM); IEEE, 2025.

(21) Kamiya, T.; Nomura, K.; Hosono, H. Present Status of Amorphous In−Ga−Zn−O Thin-Film Transistors. *Sci. Technol. Adv. Mater.* **2010**, *11*, No. 044305.

(22) Nomura, K.; Ohta, H.; Takagi, A.; Kamiya, T.; Hirano, M.; Hosono, H. Room-Temperature Fabrication of Transparent Flexible Thin-Film Transistors Using Amorphous Oxide Semiconductors. *Nature* **2004**, *432*, 488−492.

(23) Yeon, H.-W.; Lim, S.-M.; Jung, J.-K.; Yoo, H.; Lee, Y.-J.; Kang, H.-Y.; Park, Y.-J.; Kim, M.; Joo, Y.-C. Structural-Relaxation-Driven Electron Doping of Amorphous Oxide Semiconductors by Increasing the Concentration of Oxygen Vacancies in Shallow-Donor States. *NPG Asia Mater.* **2016**, *8*, No. e250.

(24) Yeon, H.-W.; Jo, J.; Song, H.; Kang, Y.; Na, S.; Yoo, H.; Lee, S.; Cho, H.; Kang, H.; Jung, J.; Han, S.; Kim, M.; Joo, Y.-C. Cu Diffusion-Driven Dynamic Modulation of the Electrical Properties of Amorphous Oxide Semiconductors. *Adv. Funct. Mater.* **2017**, *27*, No. 1700336.

(25) Moon, T. W.; Yoon, S. H.; Chung, U. J.; Park, S. Y.; Jeong, J. K. Enhanced Reliability of High-Quality a-IGZO TFTs for Micro-LED Backplanes: Mitigating V_{TH} Instability at Elevated Temperatures. *ACS Appl. Mater. Interfaces* **2025**, *17*, 14201−14210.

(26) Lim, S.-M.; Yeon, H.-W.; Lee, G.-B.; Jin, M.-G.; Lee, S.-Y.; Jo, J.; Kim, M.; Joo, Y.-C. Thermally Stable Amorphous Oxide-Based Schottky Diodes through Oxygen Vacancy Control at Metal/Oxide Interfaces. *Sci. Rep.* **2019**, *9*, No. 7872.

(27) Han, W. H.; Chang, K. J. Subgap States near the Conduction-Band Edge due to Undercoordinated Cations in Amorphous In-Ga-Zn-O and Zn-Sn-O Semiconductors. *Phys. Rev. Appl.* **2016**, *6*, No. 044011.

(28) Kim, J.; Bang, J.; Nakamura, N.; Hosono, H. Ultra-Wide Bandgap Amorphous Oxide Semiconductors for NBIS-Free Thin-Film Transistors. *APL Mater.* **2019**, *7*, No. 021101.

(29) Han, W. H.; Oh, Y. J.; Chang, K. J.; Park, J. S. Electronic Structure of Oxygen Interstitial Defects in Amorphous In-Ga-Zn-O Semiconductors and Implications for Device Behavior. *Phys. Rev. Appl.* **2015**, *3*, No. 044008.

(30) Prasai, K.; Biswas, P.; Drabold, D. A. Electrons and Phonons in Amorphous Semiconductors. *Semicond. Sci. Technol.* **2016**, *31*, No. 073002.

(31) Sankey, O. F.; Niklewski, D. J. Ab Initio Multicenter Tight-Binding Model for Molecular-Dynamics Simulations and Other Applications in Covalent Systems. *Phys. Rev. B* **1989**, *40* (6), No. 3979.

(32) Hwang, S.; Lee, J. H.; Woo, C. H.; Lee, J. Y.; Cho, H. K. Effect of Annealing Temperature on the Electrical Performances of Solution-Processed InGaZnO Thin Film Transistors. *Thin Solid Films* **2011**, *519*, 5146−5149.

(33) Moon, M. R.; Na, S.; Jeon, H.; An, C.; Park, K.; Jung, D.; Kim, H.; Lee, Y.-B.; Lee, H.-J. Effects of Substrate Heating on the Amorphous Structure of InGaZnO Films and the Electrical Properties of Their Thin Film Transistors. *Appl. Phys. Express* **2010**, *3*, No. 111101.

(34) Ide, K.; Nomura, K.; Hiramatsu, H.; Kamiya, T.; Hosono, H. Structural Relaxation in Amorphous Oxide Semiconductor, a-In-Ga-Zn-O. *J. Appl. Phys.* **2012**, *111*, No. 073513.

(35) Jang, H.; Kim, T.; Lee, W.; Cho, M.; Ha, D.; Alam, M. A.; Ye, P. D.; Jeong, C. $InGaZnO_4$ and In_2O_3 Mobility Trend: The Role of Structural Disorder from Amorphous to Crystalline States. *ACS Mater. Lett.* **2025**, *7*, 2024−2030.

(36) Kim, T.; Jang, H.; Park, B.; Shin, S.; Alam, M. A.; Ye, P. D.; Jeong, C. Engineering Amorphous IGZO Thin-Film Transistors: The Role of Composition and Channel Thickness in Mobility-Threshold Voltage Optimization. *ACS Omega* **2025**, *10* (50), 62182−62188.

(37) Smidstrup, S.; Markussen, T.; Vancraeyveld, P.; Wellendorff, J.; Schneider, J.; Gunst, T.; Verstichel, B.; Stradi, D.; Khomyakov, P. A.; Vej-Hansen, U. G.; Lee, M.-E.; Chill, S. T.; Rasmussen, F.; Penazzi, G.; Corsetti, F.; Ojanperä, A.; Jensen, K.; Palsgaard, M. L. N.; et al. QuantumATK: an integrated platform of electronic and atomic-scale modelling tools. *J. Phys.: Condens. Matter* **2020**, *32* (1), No. 015901.

(38) Kresse, G.; Furthmüller, J. Efficient Iterative Schemes for Ab Initio Total-Energy Calculations Using a Plane-Wave Basis Set. *Phys. Rev. B* **1996**, *54*, No. 11169.

(39) Kavanagh, S. R.; Squires, A. G.; Nicolson, A.; Mosquera-Lois, I.; Ganose, A. M.; Zhu, B.; Brlec, K.; Walsh, A.; Scanlon, D. O. doped: Python toolkit for robust and repeatable charged defect supercell calculations. *J. Open Source Software* **2024**, *9*, No. 6433.

(40) Kang, Y.; Ahn, B. D.; Song, J. H.; Mo, Y. G.; Nahm, H. H.; Han, S.; Jeong, J. K. Hydrogen Bistability as the Origin of Photo-Bias-Thermal Instabilities in Amorphous Oxide Semiconductors. *Adv. Electron. Mater.* **2015**, *1*, No. 1400006.

(41) Li, H.; Guo, Y.; Robertson, J. Oxygen Vacancies and Hydrogen in Amorphous In-Ga-Zn-O and ZnO. *Phys. Rev. Mater.* **2018**, *2*, No. 075001.